Lifetime evaluation of concrete structures under sustained post-peak loading

Lifetime evaluation of concrete structures under sustained post-peak loading

Fabrizio Barpi[1] and Silvio Valente[2]

[1]Dipartimento di Ingegneria Strutturale, Edile e Geotecnica, Politecnico di Torino, Corso Duca degli Abruzzi 24, 10129 Torino, Italy. E-mail: *fabrizio.barpi@polito.it*

[2]Dipartimento di Ingegneria Strutturale, Edile e Geotecnica, Politecnico di Torino, Corso Duca degli Abruzzi 24, 10129 Torino, Italy. E-mail: *silvio.valente@polito.it*

Keywords Cohesive model, concrete, crack, creep, dam, fracture, failure lifetime

Abstract *Experimental tests on crack propagation in concrete under constant post-peak loading are simulated using the finite element method and the cohesive crack model, in both Mode I and Mixed-mode conditions. The time-dependent behaviour of concrete in the process zone is due to the interaction and growth of microcracks, a phenomenon which, for high constant load levels, turns out to be predominant over linear viscoelastic creep in the bulk material. In mechanical systems based on this type of material behaviour (creep and strain-softening taking place simultaneously), the initial value problem is non-parabolic, i.e., the error at one time level is affected by the accumulation of errors introduced at earlier time levels. Despite these difficulties, the scatter in numerical failure lifetime vs. load level turns out to be negligible in Mode I conditions and practically acceptable in Mixed-mode conditions. Therefore the time-dependent behaviour of the process zone can be inferred solely from the results of direct tensile tests.*

1 INTRODUCTION

The numerical analysis of crack propagation in concrete under constant post-peak loading requires the solution of two phases: monotone static loading (Crack Mouth Opening Displacement (CMOD) rate always positive) and cyclic loading (CMOD rate negative during the unloading stage, otherwise positive). Before the beginning of the unloading stage, in fact, the system behaves in monotone static conditions and, for high reloading levels, it behaves as if it were subjected to a single unloading and reloading cycle. In this study the first phase is addressed through the *cohesive crack model* [1, 2, 3]. According to this model, the process zone can be represented as an extended portion of the real crack (or traction-free crack), called fictitious crack, where the material, albeit damaged, can still transfer stresses which are a decreasing function of the crack opening displacement (see Fig. 1).

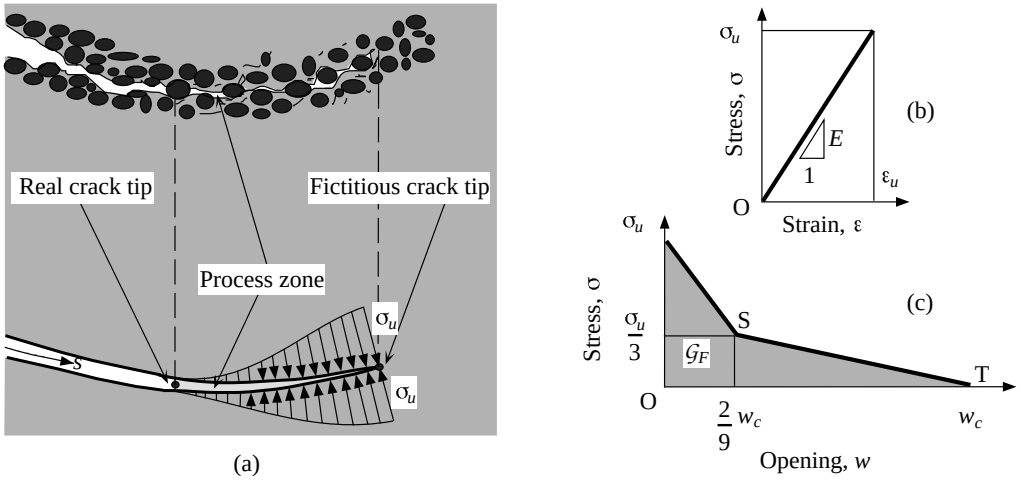

Figure 1: Process zone (a) and constitutive laws for: (b) the undamaged material and (c) the process zone.

This is a well established approach to the fracture mechanics of quasi-brittle materials because it can explain the *size-effects* observed experimentally in structural response in terms of:

- maximum load,
- softening branch slope (global brittleness),
- process zone length,
- formation of a second crack,

in both Mode I problems [4] and Mixed-mode problems [5, 6, 7, 8].

The second phase is addressed through the Focal Point Model suggested by Yankelevsky and Reinhardt [9]. Account taken of the two above mentioned phases, the *time dependent* behaviour of the process zone has been analysed [10]. It can be ascribed to the interaction and growth of the microcracks, a phenomenon which, for high constant load levels, turns out to be predominant over linear viscoelastic creep in the bulk material [11].

2 LOADING PROCEDURE

The experimental tests described in this paper can be grouped as follows:

- type A: stable tensile tests performed on cylindrical specimens, 10cm in diameter and 20cm high, with a 1cm deep notch (Fig. 2),
- type B: three-point bending tests performed according to the RILEM recommendations on prism shaped specimens, sized $10 \times 10 \times 84$cm (testing span 80cm), with a 5cm deep notch (static case) or a 2cm deep notch (creep case), see Fig. 3.
- type C: tests on planar pre-notched (notch depth 30cm) gravity dam models (Fig. 4). The geometric scale ratio between model and prototype was assumed to be $S_\ell = 1 : 40$ (2.40m (dam model height)/96m (real dam height)). The scale adopted for density was $S_\varrho = 1$, while the scale for stresses was $S_\sigma = 1$ (same value for both the model and the prototype). Having established the scales of two independent quantities (length and stress), the scales of the other quantities playing a role in static problems are determined according to Buckingham's theorem. By applying this theorem, we get the scale of volume forces as $S_g = S_\sigma/(S_\varrho S_\ell) = 40$. For this reason, it was necessary to simulate a dead-weight increment (40 times) by means of a system of discrete vertical forces [12]. The total volume of the model was subdivided into elementary portions and the equivalent forces to be applied were estimated. In order to check each vertical force applied, a spring-dynamometer is used. As shown in Fig. 4, each dynamometer is connected to a steel framework placed under the foundation of the dam. In order to disturb the static behaviour of the model as little as possible, in the fracture zone the vertical forces are applied through glued metallic plates.The hydraulic thrust was generated by means of a servocontrolled actuator (2000kN capacity) applied to the upstream side. This force was distributed in four concentrated loads whose intensity is indicated in Fig. 15. The test was carried out by controlling CMO at a rate of 1.2 μm/s.

Type A and B tests were performed at the ENEL-CRIS. laboratories of Milan [13, 14], type C tests at the ISMES laboratories of Bergamo [15, 16, 17].

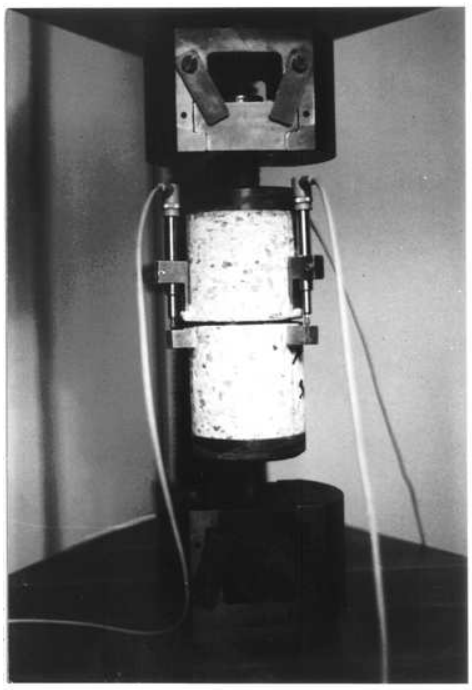

Figure 2: Tensile test setup.

The same loading procedure, consisting of the following five stages, was used in all three cases (Fig. 5):

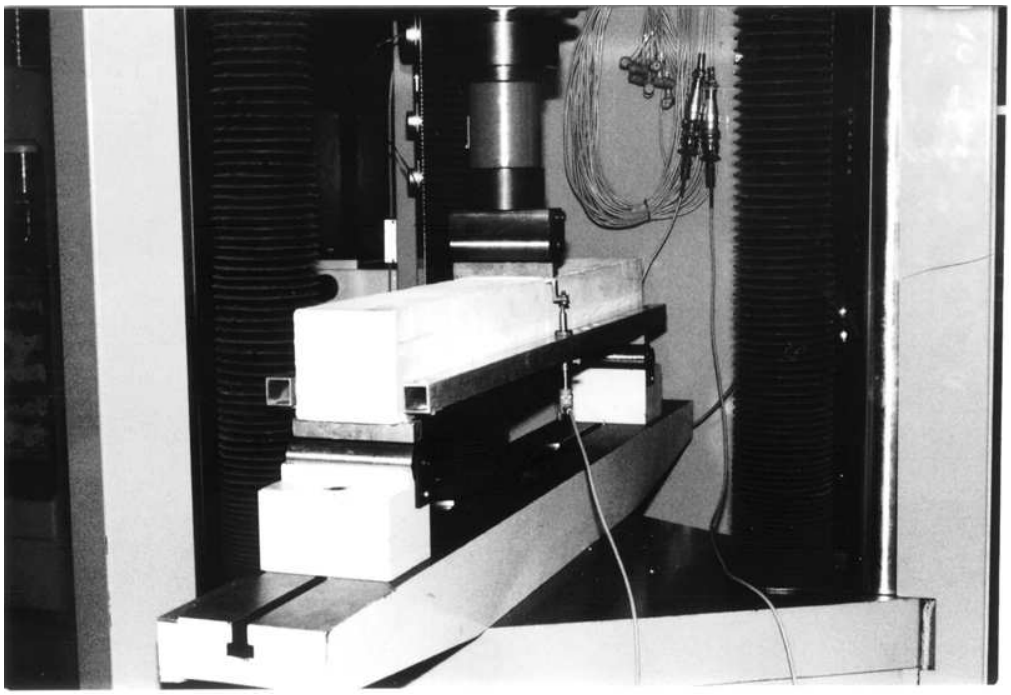

Figure 3: Three-point bending test setup.

- CMOD-controlled loading from zero to the maximum value (P_{max}),
- CMOD-controlled softening to point D,
- load-controlled unloading to point E ($P_E \approx P_{max}/10$),
- load-controlled reloading up to point G,
- constant load ($P = P_G$) until specimen failure. Since this stage is started after reaching the peak load (P_{max}), this is known as the *post-peak* test.

From a qualitative viewpoint, the load vs. CMOD diagram obtained from type B tests is similar to the one depicted in Fig. 5 (type A test). In either case, in fact, the dead-weight of the structure does not tend to close the crack and hence, when the outer load becomes negligible ($P \approx P_E$), the crack stays open. On the contrary, during type C tests, dead-weight (increased 40 times for the sake of similitude) tends to close the crack (Figs. 16, 17 and 18).

3 CONCRETE CHARACTERISATION

3.1 Static properties

From now on we shall refer to four types of concrete. The specimens and the models were stored at 20°C and 95% relative humidity, and were tested at 20°C and 50% relative humidity. Mean compressive strength was measured on six $15 \times 15 \times 15$cm cubes and Young's modulus on two $15 \times 15 \times 60$cm prisms; fracture energy was determined through type B tests, and tensile strength through type A tests. By way of an exception, for the first concrete type listed in Table 1 (maximum aggregate size $\phi = 10$mm), the elastic modulus was determined by having the numerical solution best fit the test results relating to the initial portion of the P vs. CMOD curve. Mean static concrete properties are summarised in Table 1.

The numerical simulations were performed on the basis of the properties listed in Table 1, assuming a Poisson's ratio of 0.1.

Table 1: Mean static concrete properties.

Test series ϕ (mm)	Mean compr. strength (MPa)	Concr. age at test (T) (Months)	Mean Young's modulus (E) (at T months) (MPa)	Mean fracture energy (at T months) (N/m)	Mean tens. strength (at T months) (MPa)
10	42	6	38.0	132.00	2.500
3.15	32	8	22.1	96.55	1.950
12	28	8	28.0	141.15	2.375
25	35	8	35.2	121.49	2.885

3.2 Unloading and reloading stages

In order to determine the state of stress in the fictitious process zone (FPZ), it proves necessary to resort to a constitutive law for the unloading and reloading stages. As suggested in [18], the numerical simulations were performed by using the Focal Point Model [9], which is described in schematic form in Fig. 6.

It is characterised by a marked curvature in the initial portion of the unloading branch and by the fact that it joins the static curve at a point characterised by a stress lower than the starting stress ($\sigma_M < \sigma_A$).

The entire potential unloading, or reloading, polygonal turns out to be defined as soon as its initial point is defined. This does not necessarily occur simultaneously for all the cohesive elements.

3.3 Creep stage

The creep law adopted is the one proposed in [13], which is based on the following observations concerning type A tests:

- for the four concrete types analysed, the relationship between the load level, P_G/P_D, and failure lifetime, t_{cr}, can be best fitted by a power law, as shown in Fig. 7.
- Fig. 8 shows the normalised creep COD (defined as $\frac{w^c}{w^c_{ult}} = \frac{w-w_G}{w_H-w_G}$, see Fig. 5) vs. normalised time (t/t_{cr}) curves. For each type of concrete, the difference between such curves at different load levels (P_G/P_D) turned out to be not greater than the difference between different tests at the same level. As a result, this relationship was taken to be unique.

The best-fitting curves shown in Fig. 8 were obtained by assuming the creep related COD rate to depend on three terms (Eqs. 2), relating to *primary*, *secondary* and *tertiary* creep. During the constant load (P_G) stage of stable tensile tests (referred to as type A tests), it is assumed that the tensile stress (σ_G) is the same at all points of the process zone and does not vary over time. In this manner it becomes possible to characterise the time-related behaviour of the process zone formed in a given type of concrete.

Equation 1 is proposed to best fit the mean creep curves:

$$\frac{\mathrm{d}(\frac{w^c}{w^c_{ult}})}{\mathrm{d}(\frac{t}{t_{cr}})} = \Phi\left(\frac{w^c}{w^c_{ult}}\right) = c_1\, e^{\left(-50\frac{w^c}{w^c_{ult}}\right)} + c_2 + c_3\left(\frac{w^c}{w^c_{ult}}\right)^5. \tag{1}$$

Coefficients c_1, c_2, c_3 are determined by a numerical integration of Eq. 1 in order to best fit the mean creep curves (see Fig. 8). According to a phenomenological approach, Eq. 1 is assumed as a constitutive law for the process zone.

By taking into account the results shown in Fig. 7 and 8 it is possible to rewrite Eq. 1 for the four materials analised.

$$
\begin{aligned}
\frac{\dot{w}^c}{w^c_{ult}} &= 9.60\times10^{-3}\left(\frac{\sigma_G}{\sigma_D}\right)^{27}\left[0.556+4.45\,\mathrm{e}^{\left(-50\frac{w^c}{w^c_{ult}}\right)}+10.2\left(\frac{w^c}{w^c_{ult}}\right)^5\right], && \phi = 10\text{mm}\\
\frac{\dot{w}^c}{w^c_{ult}} &= 9.71\times10^{-3}\left(\frac{\sigma_G}{\sigma_D}\right)^{27}\left[0.450+35\,\mathrm{e}^{\left(-50\frac{w^c}{w^c_{ult}}\right)}+12\left(\frac{w^c}{w^c_{ult}}\right)^5\right], && \phi = 3.15\text{mm}\\
\frac{\dot{w}^c}{w^c_{ult}} &= 6.90\times10^{-3}\left(\frac{\sigma_G}{\sigma_D}\right)^{26}\left[0.400+9\,\mathrm{e}^{\left(-50\frac{w^c}{w^c_{ult}}\right)}+25\left(\frac{w^c}{w^c_{ult}}\right)^5\right], && \phi = 12\text{mm}\\
\frac{\dot{w}^c}{w^c_{ult}} &= 16.72\times10^{-4}\left(\frac{\sigma_G}{\sigma_D}\right)^{19}\left[0.350+15\,\mathrm{e}^{\left(-50\frac{w^c}{w^c_{ult}}\right)}+32\left(\frac{w^c}{w^c_{ult}}\right)^5\right], && \phi = 25\text{mm}
\end{aligned}
\tag{2}
$$

By introducing such properties into the cohesive model, three-point bending tests and tests on gravity dam models were simulated.

3.4 Constant load stage

During stage 5, the external load is kept constant and because of the relaxation of the process zone the stress path extends from point G to the static envelope (Fig. 9, left). In the numerical simulations, the latter was simulated by means of Petersson's bilinear curve [19].

According to the integration procedure proposed by Zhou [10], any time increment can be divided into two steps (Fig. 9, right):

- during time $\mathrm{d}t$, w is kept constant, and a relaxation stress $\mathrm{d}\sigma^R = -F\,\dot{w}^c\,\mathrm{d}t$ develops in the process zone (the COD rate is given by Eqs. 2),
- the reduction in the closing cohesive stresses acting on the edges of the fictitious crack causes an increase in crack opening, $\mathrm{d}w$, and an increase in stress, $\mathrm{d}\sigma^I$, in each cohesive element.

In stage 5, unlike stages 3 and 4, the stress path does not depend solely on the definition of its initial point G, but also on the evolution of displacements over time. In Fig. 9 the sequence of steps is magnified for the sake of clarity; in actual fact, the steps are limited so that it is $|\mathrm{d}\sigma^R| < \sigma/100$ and $\mathrm{d}w < w^c_{ult}/100$. Upon reaching the static envelope, the stress path is forced to follow it ($\mathrm{d}w/\mathrm{d}t > 0$).

4 COHESIVE CRACK MODEL

According to the finite element method, keeping in mind that the constitutive law for the FPZ is piecewise linear, by taking the unknowns to be the n nodal displacement increments, $\mathrm{d}\boldsymbol{u}$, and assuming that compatibility and equilibrium conditions are satisfied at all points in the solid, we get the following system of n equations with $n+1$ unknowns ($\mathrm{d}\boldsymbol{u}$, $\mathrm{d}\lambda$ or $\mathrm{d}t$). The creep effect is incorporated by simply adding the pseudo–load caused by relaxation to the load vector in the equilibrium equations [14, 16]:

$$
(\boldsymbol{K}_T + \boldsymbol{C}_T)\,\mathrm{d}\boldsymbol{u} = \mathrm{d}\lambda\,\boldsymbol{P} + \mathrm{d}t\,\boldsymbol{Q}, \tag{3}
$$

where:

- $\boldsymbol{K}_T$: positive definite tangential stiffness matrix, containing contributions from linear elastic elements and possible contributions from cohesive elements with values (σ_c, w_n) inside the static envelope [phases (3), (4) and (5)];

- $\boldsymbol{C}_T$: negative definite tangential stiffness matrix, containing contributions from cohesive elements with values (σ_c, w_n) on the static envelope [phases (1), (2) and some elements during phase (5)];
- $\boldsymbol{P}$ is the vector of hydrostatic load normalised in order to obtain $\sum P_i = 1$ (see Fig. 15, right);
- $\mathrm{d}\lambda$ maximum load multiplier which is compatible with all active limits.
- $\boldsymbol{Q}$: vector of the unbalanced load (or pseudo–load) due to relaxation in the process zone, related to a unitary time increment;
- $\mathrm{d}t$: maximum time increment which is compatible with all active limits (see also $\mathrm{d}\lambda$).

The displacements, $\boldsymbol{u}$, are related to the process zone and to the loading points. For purposes of numerical efficiency, the remaining displacements are statically condensed. The nodes on the crack are split and connected by a two-node element orthogonal to the crack. These elements, which are mutually independent, follow the constitutive law for the process zone. During stages 1, 2, 3 and 4, the behaviour of the material is assumed to be time independent ($\boldsymbol{Q} = \boldsymbol{0}$) and hence the external load changes ($\mathrm{d}\lambda \neq 0$ and $\mathrm{d}t = 0$). On the contrary, during stage 5, the behaviour of the process zone is assumed to be time dependent ($\boldsymbol{Q} \neq \boldsymbol{0}$) and the external load is kept constant ($\mathrm{d}\lambda = 0$ and $\mathrm{d}t \neq 0$). During the initial steps of stages 1 and 2, $\mathrm{d}\boldsymbol{u}$ and $\mathrm{d}\lambda$ are limited by a single condition: $\sigma_{FCT} \leq \sigma_u$. As a result, the Fictitious Crack Tip (FCT) is seen to spread with each step. In the later stages, the stresses in the elements farthest away from the FCT approach point S of Fig. 6, thereby activating another limiting condition on $\mathrm{d}\boldsymbol{u}$ and $\mathrm{d}\lambda$: the stress path, in fact, is now prevented from going beyond point S within a single step. The passing of point S cannot take place, in fact, unless matrix $\boldsymbol{C}_T$ is reassembled, which means it must take place in two steps.

During the unloading and reloading stages (stages 3 and 4), the main limiting condition is given by the angular points of the respective polygonals which, like point S discussed above, cannot be passed within a single step. In some cases, the fictitious crack may grow. The initial part of the constant load stage (stage 5) is subjected to the limiting conditions described above $|\mathrm{d}\sigma_R| < \sigma/100$ and $\mathrm{d}w < w^c_{ult}/100$, $\sigma_{FCT} \leq \sigma_u$, and the relaxation of the cohesive stresses may result in a growth of the fictitious crack. Later on, some of the stress paths approach the angular point H (at the intersection with the static envelope, Fig. 9) thereby giving rise to another limiting condition.

Finally, the stress paths, which move along the static envelope, entail the limiting conditions relating to points S and T (Fig. 9), as are typical of stages 1 and 2. These elements, together with the ones arising from the growth of the fictitious crack, contribute to matrix $\boldsymbol{C}_T$ ($\mathrm{d}\sigma/\mathrm{d}w < 0$); when their number becomes significant, the $\boldsymbol{K}_T + \boldsymbol{C}_T$ matrix loses its characteristic of being positive definite and the constant load may no longer be sustained. This condition determines the failure lifetime of the structure t_{cr}.

5 STABILITY OF THE INITIAL VALUE PROBLEM

Figure 10 shows the diagram of Eq. 2 after setting $\upsilon = w^c/w^c_{ult}$. For purposes of the following discussions, it is useful to express this diagram as a piecewise linear curve so as to obtain:

$$\dot{\upsilon}(t) + \alpha\, \upsilon(t) = \beta \tag{4}$$

where:

- α: parameter that controls the slope of each segment of Fig. 10 (α positive means $\dot{\upsilon}$ decreasing function of υ),

- $\beta = \dot{v}|_{v=0}$: constant parameter depending on initial conditions.

From numerical analysis [20] we know that Eq. 4 represents an initial value problem which can be classified depending on the way in which a *perturbation* of the solution at one time level affects the solution at later levels. In particular:

- $\alpha > 0$: the perturbations of the solutions *decay* with time, and perturbations originating from different time levels do not accumulate. This is the situation we are faced with during primary creep.
- $\alpha = 0$: a sort of "*non-accumulation*" of perturbations occurs. This is the situation encountered during secondary creep.
- $\alpha < 0$: this is the general case, in which the error associated with a numerical solution grows with time, since the error of one time level is affected by the *accumulation* of errors introduced at earlier time levels. This situation occurs during tertiary creep.

In the first two cases the problem is classified as *parabolic*.

The diagram shown in Fig. 10 refers to a system with a single degree of freedom, as is used to represent direct tensile tests in schematic form (type A tests). Type B and C tests, instead, are represented by means of mechanical systems with several degrees of freedom. In such circumstances, the v ratio in Eq. 4 is replaced with a vector $\boldsymbol{V}$ with as many components as the points used to discretise the process zone. Similarly, the scalar quantity α is replaced with matrix $\boldsymbol{A}$. There is no accumulation of errors, and hence the system can be classified as parabolic if and only if $\boldsymbol{A}$ is *symmetric positive semidefinite* [20].

During the numerical simulation it was observed that the the overall system retains its parabolic character at the beginning of the crack propagation process only. As the fictitious crack tip grows, the smallest eigenvalue of $\boldsymbol{K}_T + \boldsymbol{C}_T$ decreases undermining the parabolic nature of the global response, even when the local constitutive law (Eq. 4) is still in a parabolic phase.

6 NUMERICAL SIMULATIONS

6.1 Three-point bending tests

The finite element mesh used in the numerical simulations of three-point bending tests is illustrated in Fig. 11. Each triangular element has been further subdivided into four constant strain triangles by joining the midpoints of the sides. The concrete employed is the one characterised by 10mm max. aggregate size, whose properties are given in Table 1 and Eq. (1a).

Figure 12 shows the load vs. CMOD diagrams for $P_{max}/P_D = 1.926$ and $P_G/P_D = 0.90$. The experimental and the numerical curves are in good agreement and suggest that the collapse of the specimen takes place when the $(P, CMOD)$ point reaches the static curve, which therefore behaves as an envelope curve. This conclusion is confirmed by the results obtained for other values of P_G/P_D and P_{max}/P_D.

Figures 12, 13 and 14 show that the numerical results are in good agreement with the experimental findings. In this case, any variation in P_G/P_D, even a very small one (for example < 0.001), may result in the static envelope being reached by the cohesive elements according to a different sequence. This fact represents a perturbation of the solution, which, on account of the non-parabolic nature of the system of equations, will tend to increase, giving rise to a non continuous correlation between failure lifetime and the load level.

This phenomenon cannot be appreciated graphically in the diagram shown in Fig. 13, but it can be seen in Fig. 14 for high values of P_G/P_D; it is negligible for practical design purposes.

6.2 Gravity dam models

The finite element mesh used for the three gravity dam models is illustrated in Fig. 15. Each element is a linear strain triangle with six nodes.

Before stage 1 (CMOD rate of 0.03μm/s) starts, the vertical load is applied, to simulate the dead-weight increment required ($S_g = 40$). In order to prevent concrete damage in compression, two plastic sheets (0.1mm thick each) and expansive mortar were placed into the notch. Negative CMOD at this step is due to the compression of the plastic sheets and to the transducer base length of 8cm. The vertical load is kept constant during all the following stages. For the numerical simulation of negative CMOD values, a bilateral contact law on the notch was adopted, i.e.:

$$\sigma = 0 \quad \text{for} \quad w \geq 0; \quad \sigma = 4.5\, w\, \frac{\sigma_u}{w_{nc}} \quad \text{for} \quad w < 0. \tag{5}$$

Figures 16, 17, 18 and 19, 20, 21 show that numerical and experimental results are in good agreement. Direct tensile tests and three-point bending tests show that the collapse occurs when the load vs. CMOD path reaches the corresponding static curve (static envelope, Figs. 5 and 12). On the contrary, experimental and numerical results related to three gravity dam models show that creep failure occurs before the static envelope is reached.

In the tests illustrated in Fig. 16, model failure occurred at the reloading stage. Therefore the experimental failure lifetime is computed from the test starting time. Figures 17 and 18 show that about 50% of peak load is required to balance the dead-weight so as obtain CMOD=0, along the first loading branch. Therefore the P_G/P_D ratios presented in Figs. 19 and 20 are not comparable with the ratios obtained in bending and tensile tests[1]. Unlike Mode I conditions, these testing conditions call for several remeshing steps during stage 5, which cause perturbations in the time integration process (see [21]). Since the system of equations is non-parabolic, an appreciable (albeit acceptable) degree of scatter is observed in failure lifetime results (Figs. 19, 20 and 21).

7 CONCLUSIONS

- From the numerical analysis of a mechanical model able to take into account simultaneously the effects of both *strain-softening* (reduction in bearing capacity as a function of strain) and *creep*, it can be seen that the effects of a perturbation increase during the subsequent time integration process. In other words, the initial value problem for such a system is non-parabolic. This behaviour is an intrinsic feature of the problem and does not depend on the creep law, the representation of damage (for example: smeared crack model or discrete crack model) or the numerical method adopted to represent the linear elastic part of the solid (for example: finite element method or boundary element method).

- The greater or lesser scatter in the results in terms of failure lifetime therefore depends on the amplitude of the perturbations affecting the mechanical system during the time integration process.

- When the crack trajectory is known a priori, as in Mode I problems, remeshing is not necessary. The perturbations therefore turn out to be *very small*, and their effects on the failure lifetime of a structure are negligible. On the contrary, remeshing (a step which proves necessary in Mixed-mode problems) represents a *perturbation* having repercussions on the failure lifetime of a structure.

- The scatter in numerical results, however, is lower than the scatter determined experimentally by repeating the same test several times, as born out by the numerous tensile

[1] It must be noticed that, because of a problem encountered during the experimental test, the model presented in Fig. 17 was unloaded/reloaded twice.

and bending test results of this kind given in the literature (see, for example, Figs. 7, 13 and 14).

- Despite these difficulties, the model discussed in this paper serves as a valid tool to predict the failure lifetime of cracked concrete structures, starting from a characterisation of the time-dependent behaviour of the process zone as inferred solely from the results of direct tensile tests. In this manner, no restrictive assumption concerning the evolution in time of the stress path at every point of the process zone is introduced.

- With reference to three-point bending tests and tests on gravity dam models, numerical and experimental results are seen to be in good agreement in terms of total load, displacements and failure lifetime.

Acknowledgments

The financial support provided by the Italian Department of University and Scientific Research (MIUR) to the research project on *"Dam-reservoir-foundation systems: dynamic, diagnostic and safety analyses"* (grant number 2002087915_006) is gratefully acknowledged.

References

[1] G.I. Barenblatt. The formation of equilibrium cracks during brittle fracture: general ideas and hypotheses. *Journal of Applied Mathematics and Mechanics*, pages 622–636, 1959.

[2] D.S. Dugdale. Yielding of steel sheets containing slits. *Journal of Mechanics and Physics of Solids*, 8:100–114, 1960.

[3] A. Hillerborg, M. Modeer, and P.E. Petersson. Analysis of crack formation and crack growth in concrete by means of fracture mechanics and finite elements. *Cement and Concrete Research*, 6:773–782, 1976.

[4] A. Carpinteri. Size effects on strength, toughness and ductility. *Journal of Engineering Mechanics (ASCE)*, 115:1375–1392, 1989.

[5] P. Bocca, A. Carpinteri, and S. Valente. Mixed-mode fracture of concrete. *International Journal of Solids and Structures*, 27:1139–1153, 1991.

[6] A. Carpinteri, S. Valente, G. Ferrara, and L. Imperato. Experimental and numerical fracture modelling of a gravity dam. In Z.P. Bažant, editor, *Fracture Mechanics of Concrete Structures*, pages 351–360, The Netherlands, 1992. Elsevier Applied Science.

[7] S. Valente, F. Barpi, G. Ferrara, and G. Giuseppetti. Numerical simulation of centrifuge tests on prenotched gravity dam models. In E. Bourdarot, J. Mazars, and V. Saouma, editors, *Dam Fracture and Damage*, pages 111–119, Rotterdam (The Netherlands), 1994. Balkema.

[8] F. Barpi and S. Valente. Size-effects induced bifurcation phenomena during multiple cohesive crack propagation. *International Journal of Solids and Structures*, 35(16):1851–1861, 1998.

[9] D.Z. Yankelevsky and H.W. Reinhardt. Uniaxial behaviour of concrete in cyclic tension. *Journal of Structural Engineering (ASCE)*, (1):166–182, 1989.

[10] F.P. Zhou. Some aspects of tensile fracture behaviour and structural response of cementitious material. Technical Report TVBM-1008, Lund University, 1988.

[11] Z.P. Bažant and Y. Xiang. Crack growth and lifetime of concrete under long time loading. *Journal of Engineering Mechanics (ASCE)*, 4:350–358, 1997.

[12] F. Barpi and S. Valente. Numerical simulation of prenotched gravity dam models. *Journal of Engineering Mechanics (ASCE)*, 126(6):611–619, 2000.

[13] A. Carpinteri, S. Valente, F.P. Zhou, G. Ferrara, and G. Melchiorri. Crack propagation in concrete specimens subjected to sustained loads. In F.H. Wittmann, editor, *Fracture Mechanics of Concrete Structures*, pages 1315–1328, Germany, 1995. Aedificatio.

[14] A. Carpinteri, S. Valente, F.P. Zhou, G. Ferrara, and G. Melchiorri. Tensile and flexural creep rupture tests on partially-damaged concrete specimens. *Materials and Structures*, 30:269–276, 1997.

[15] F. Barpi and S. Valente. Time induced crack propagation in concrete structures: cohesive crack model in mixed-mode conditions. Technical Report A845/95, Structural Engineering Department, Politecnico di Torino, 1996.

[16] F. Barpi, F. Chillè, L. Imperato, and S. Valente. Creep induced cohesive crack propagation in mixed mode. In D. Durban and J.R.A. Pearson, editors, *Non-Linear Singularities in Deformation and Flow*, pages 155–168, The Netherlands, 1999. Kluwer Academic Publishers.

[17] F. Barpi, G. Ferrara, L. Imperato, and S. Valente. Lifetime of concrete dam models under constant loads. *Materials and Structures*, 32:103–111, 1999.

[18] F. Barpi and S. Valente. Crack propagation under constant load: constitutive laws for the process zone. In R. de Borst, N. Bićanić, H. Mang, and G. Meschke, editors, *Computational Modelling for Concrete Structures*, pages 285–290, Rotterdam (The Netherlands), 1998. Balkema.

[19] P.E. Petersson. Crack growth and development of fracture zones in plain concrete and similar materials,. Technical Report TVBM-1006, Lund University, 1981.

[20] K. Eriksson, D. Estep, P. Hansbo, and C. Johnson. *Computational differential equation.* Cambridge University Press, England, 1996.

[21] S. Valente. Heuristic softening strip model in the prediction of crack trajectories. *Theoretical and Applied Fracture Mechanics*, 19:119–125, 1993.

Figure 4: Dam model test setup.

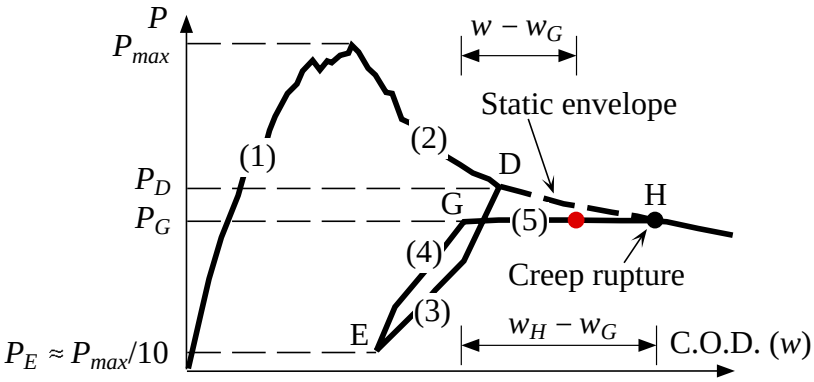

Figure 5: Loading procedure.

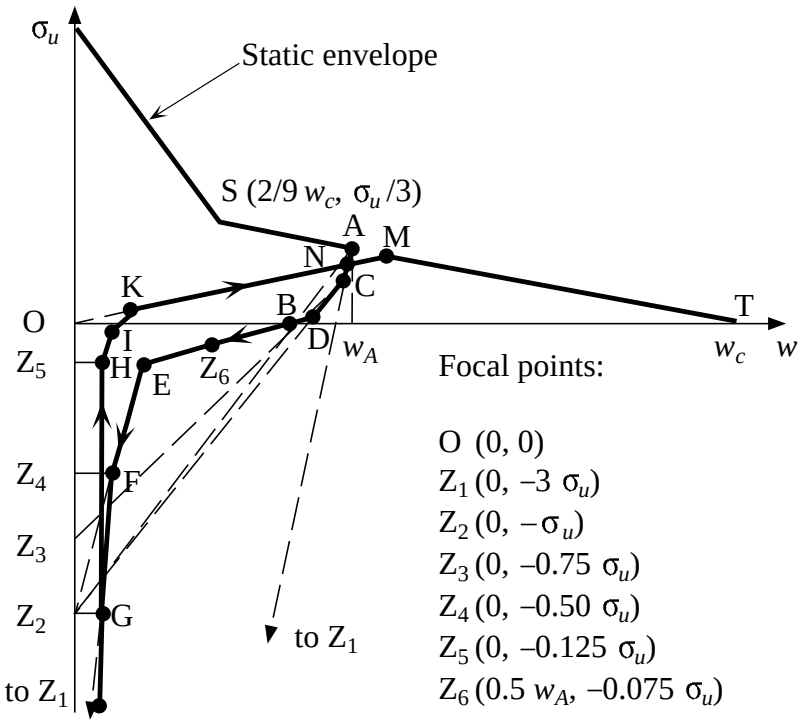

Figure 6: Focal Point Model.

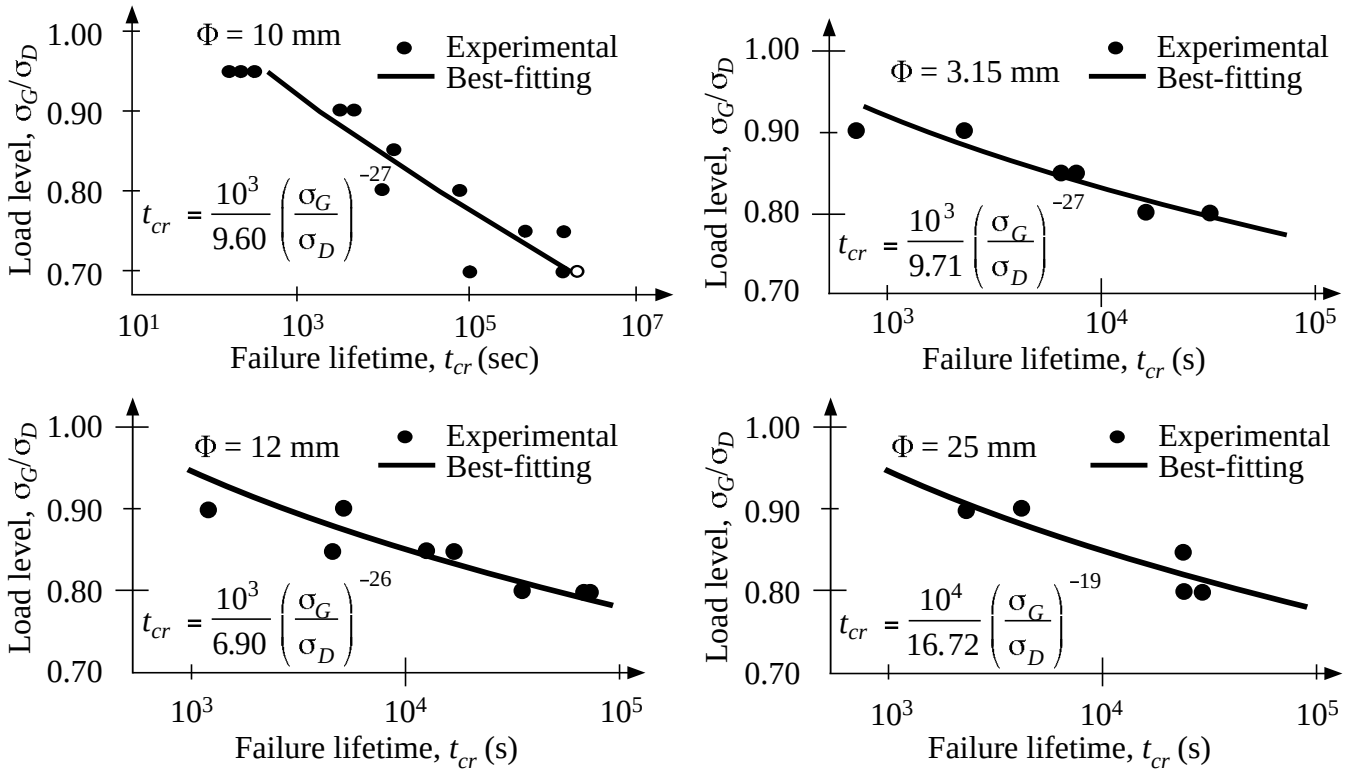

Figure 7: Load level vs. failure lifetime.

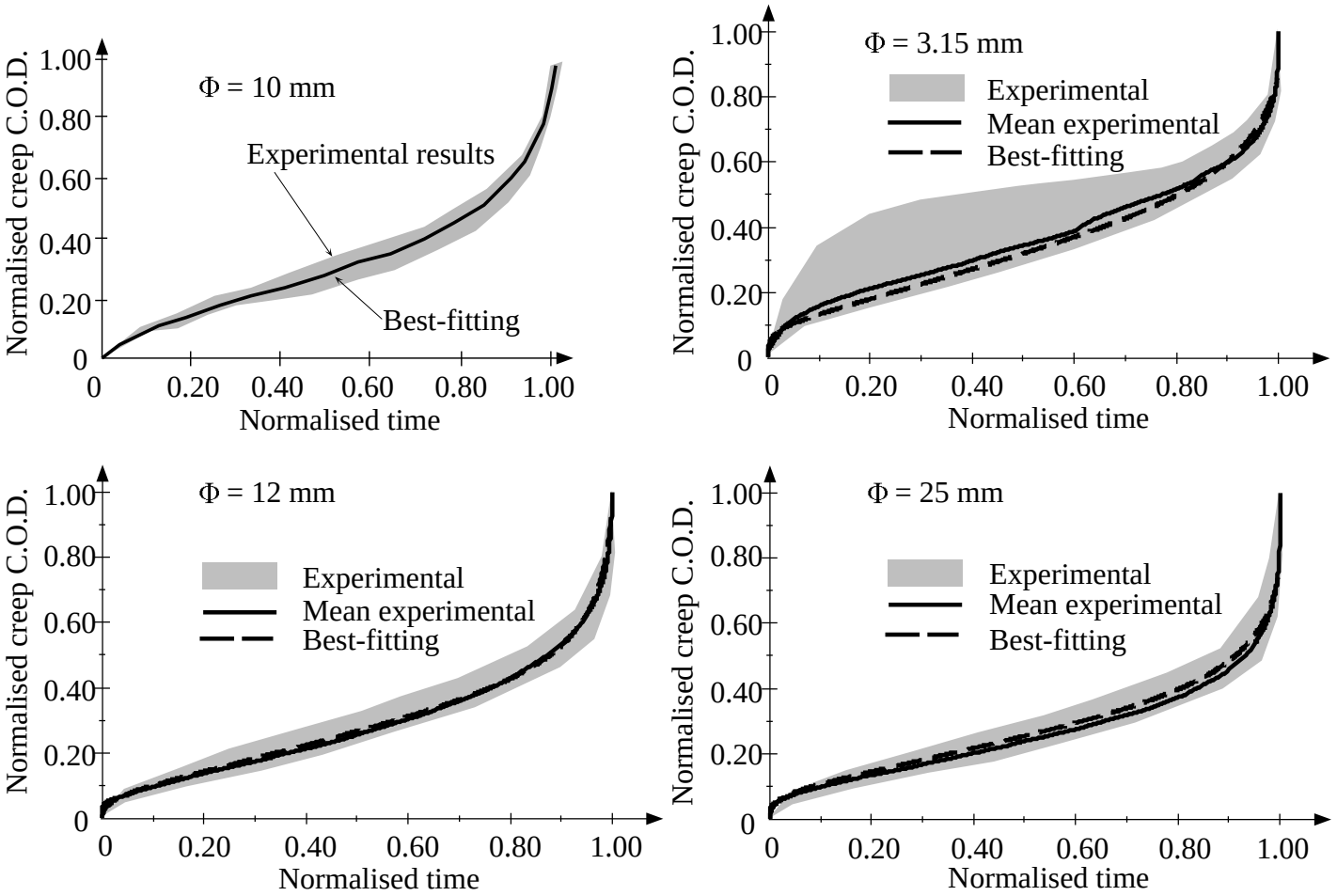

Figure 8: Normalised creep vs. normalised time.

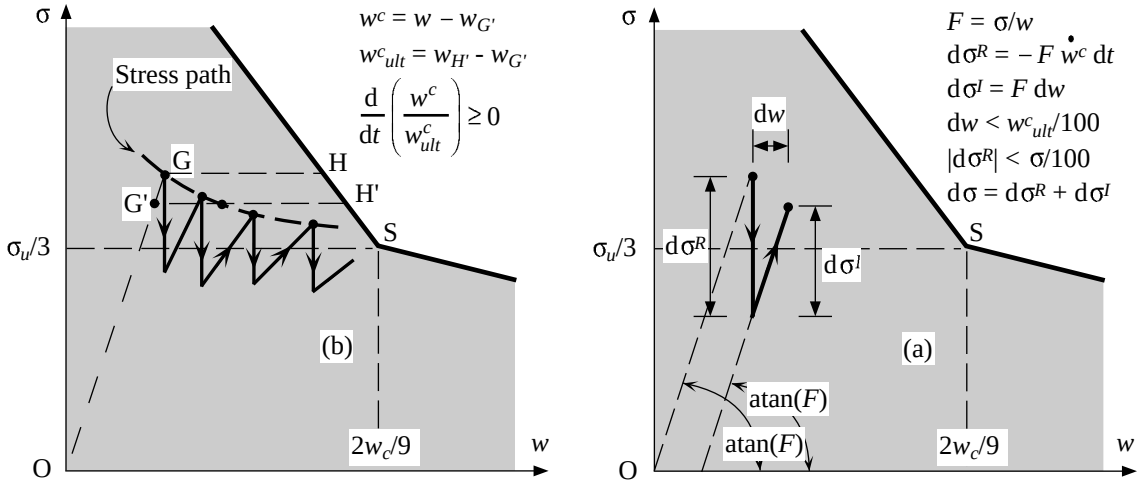

Figure 9: Stress path during creep phase: (a) integration procedure and (b) stress path.

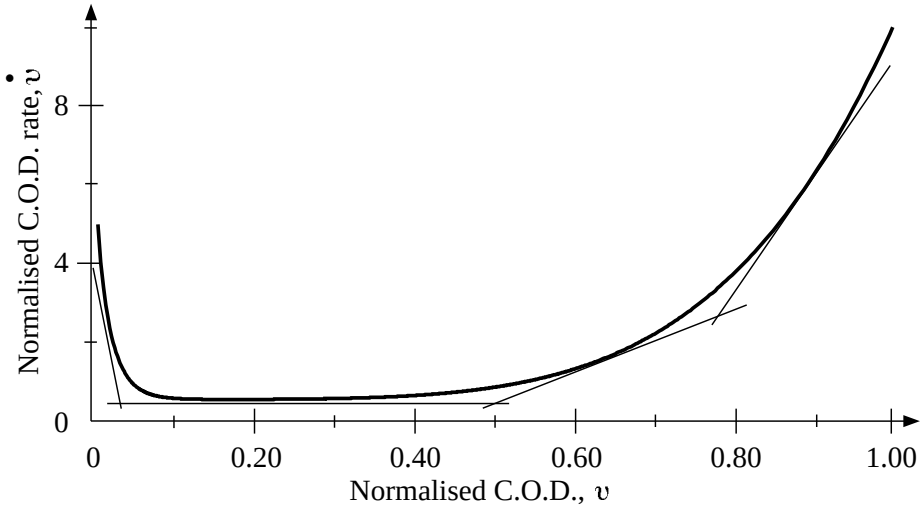

Figure 10: Creep COD rate vs. creep COD in tensile tests ($\phi = 10$mm).

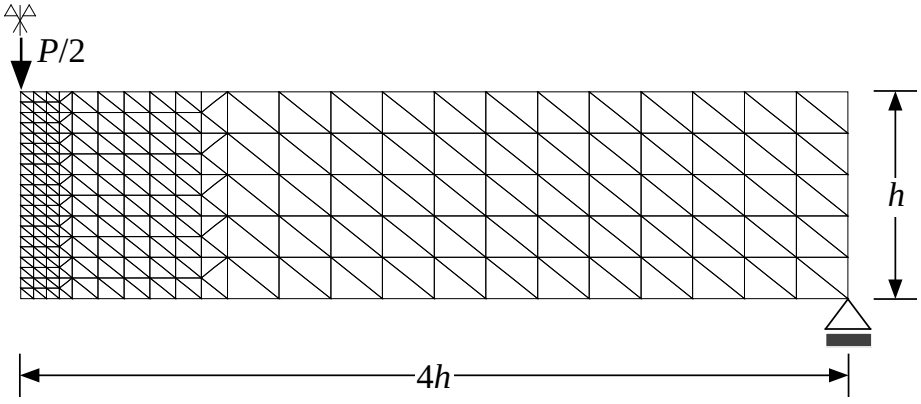

Figure 11: Half of the mesh used in the three-point bending test.

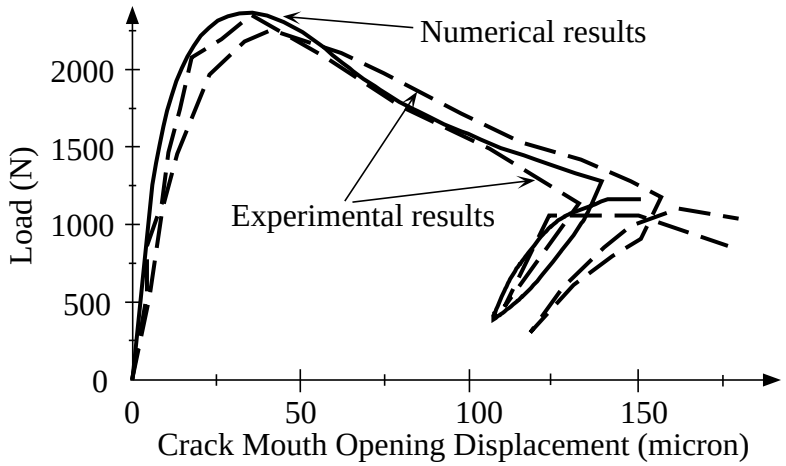

Figure 12: Load vs. CMOD (three-point bending test).

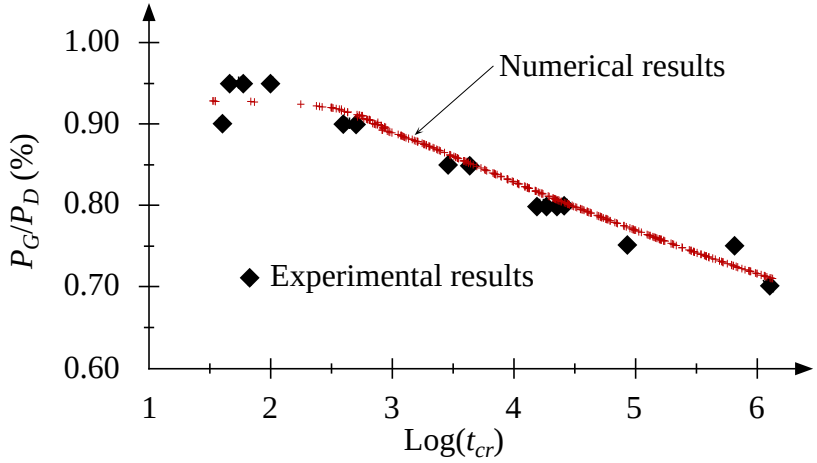

Figure 13: Load level vs. failure lifetime in bending test. High initial damage level $P_{max}/P_D = 1.926$.

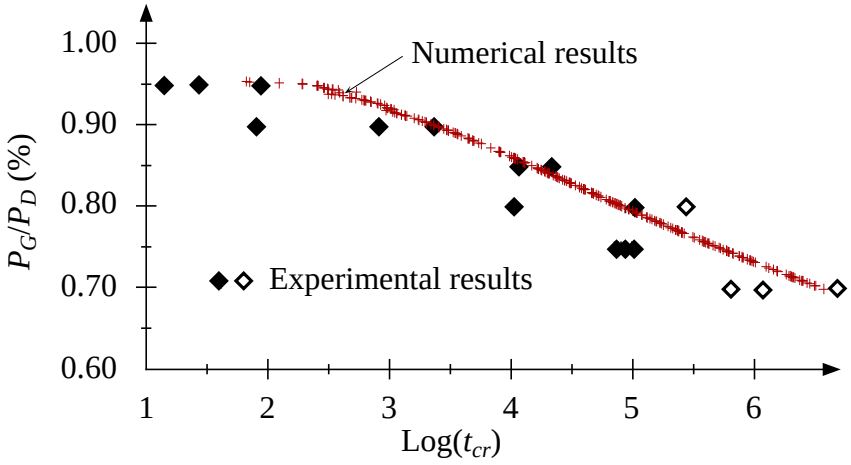

Figure 14: Load level vs. failure lifetime in bending test. Medium initial damage level $P_{max}/P_D = 1.325$ (hollow diamond dot denotes tests without final creep rupture).

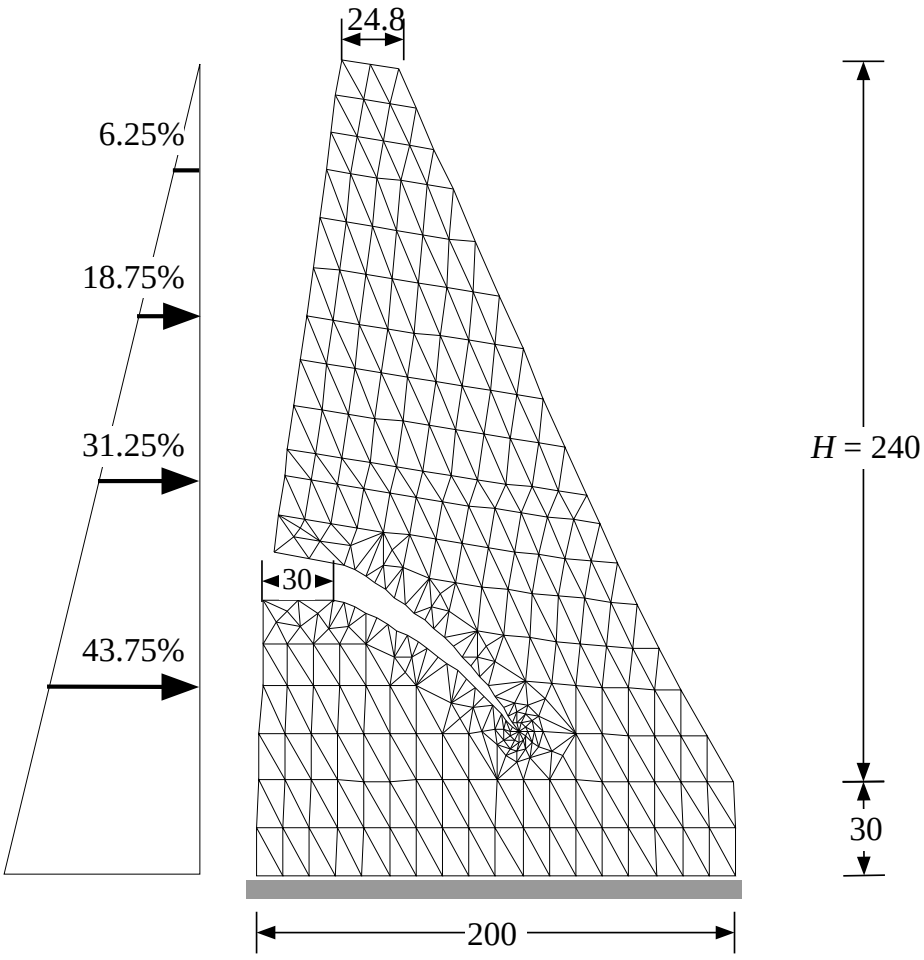

Figure 15: Deformed dam mesh (dimensions in cm).

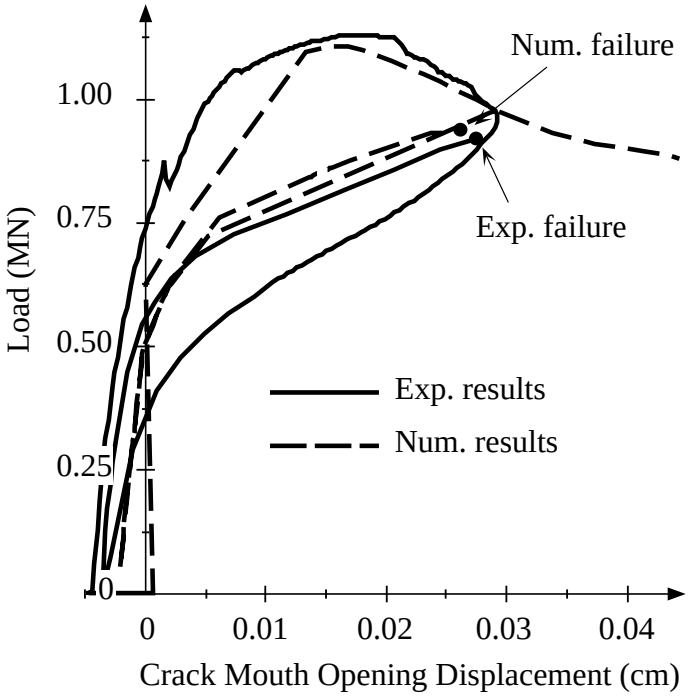

Figure 16: Load vs. CMOD (dam models, $\phi = 3.15$mm).

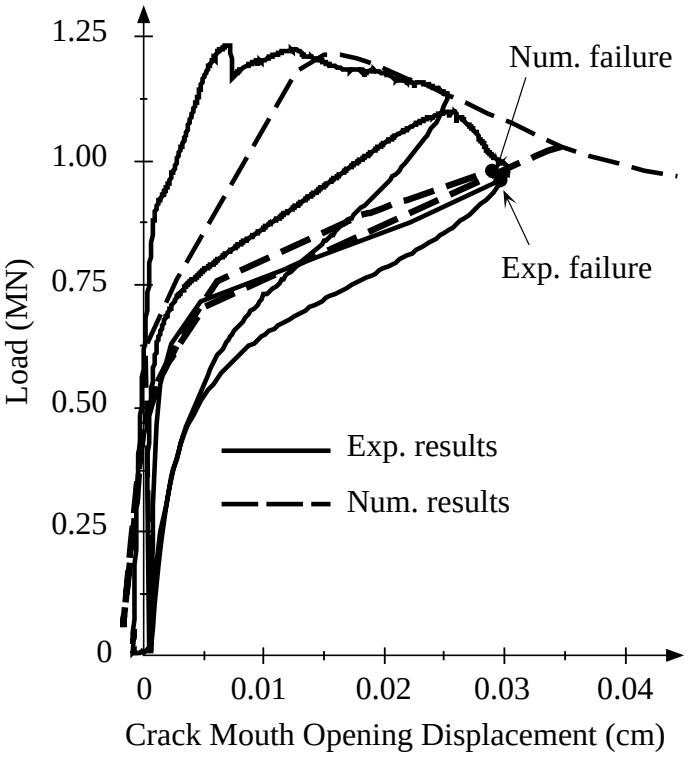

Figure 17: Load vs. CMOD (dam models, $\phi = 12$mm).

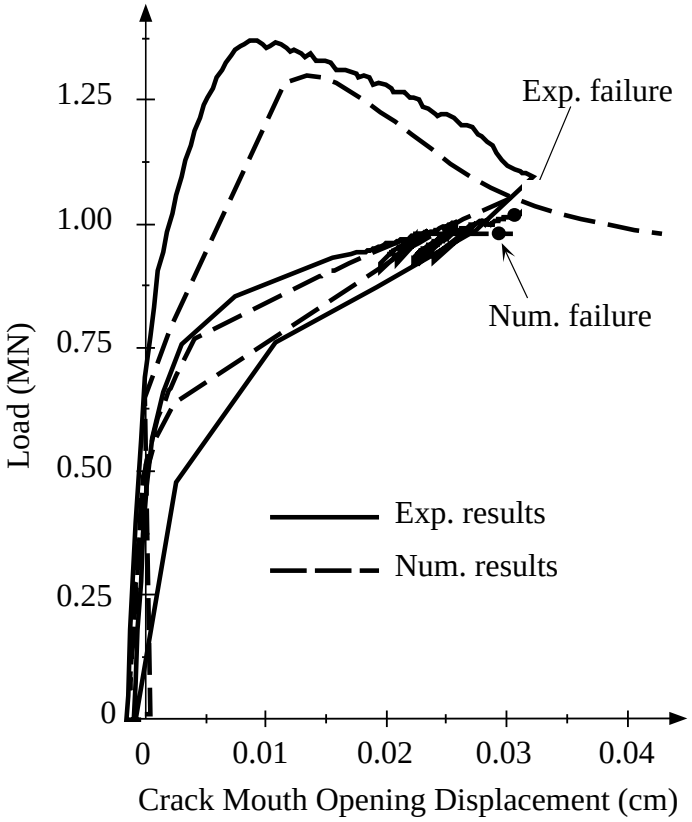

Figure 18: Load vs. CMOD (dam models, $\phi = 25$mm).

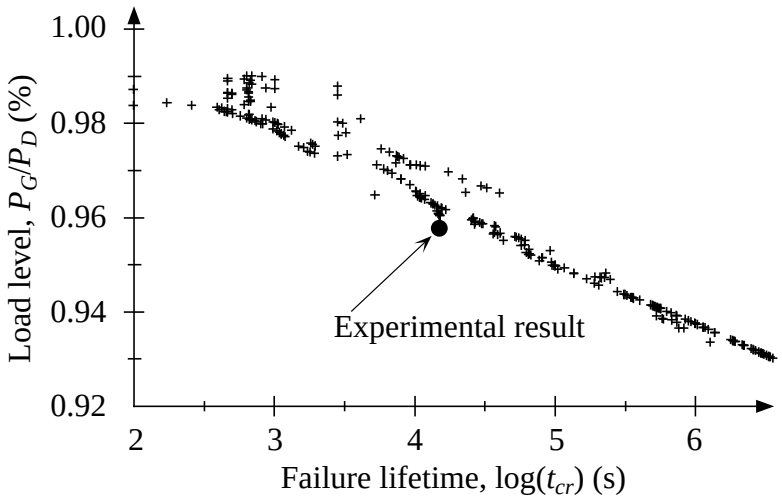

Figure 19: Load level vs. failure lifetime (dam models, $\phi = 3.15$mm).

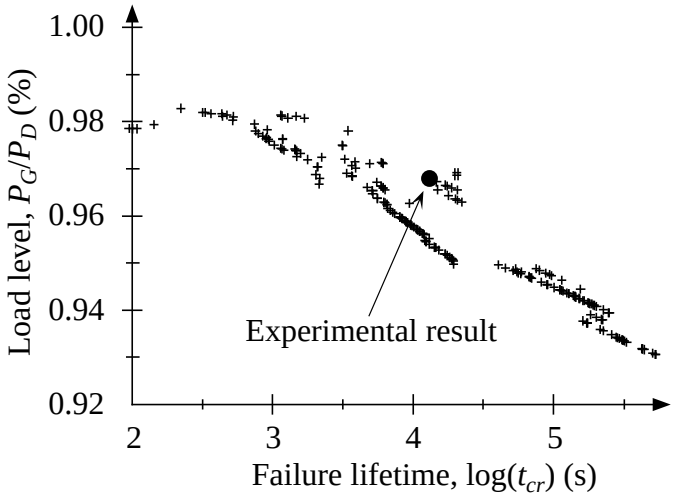

Figure 20: Load level vs. failure lifetime (dam models, $\phi = 12$mm).

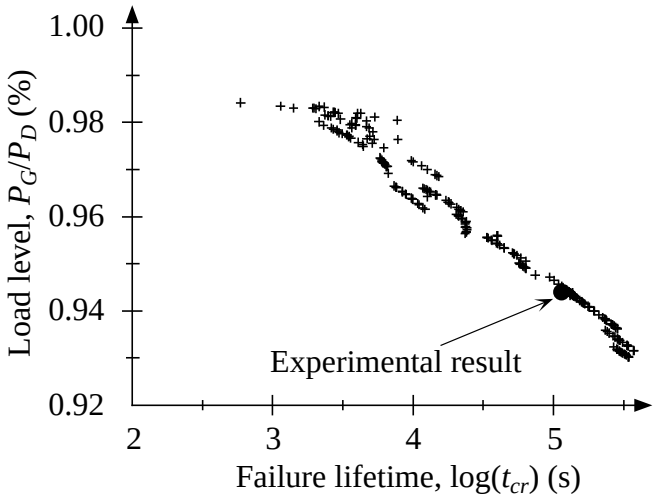

Figure 21: Load level vs. failure lifetime (dam models, $\phi = 25$mm).